Real-time investigation on the influences of vanadium additives to the structural and chemical state evolutions of LiFePO$_4$ for enhancing the electrochemical performance of lithium-ion battery

CrossMark

Chih-Wei Hu [a, b], Tsan-Yao Chen [a], Kai-Sheng Shih [b, c], Pin-Jiun Wu [b], Hui-Chia Su [b], Ching-Yu Chiang [b], An-Feng Huang [e], Han-Wei Hsieh [e], Chia-Chin Chang [d], Bor-Yuan Shew [b], Chih-Hao Lee [a, b, *]

[a] Department of Engineering and System Science, National Tsing Hua University, Hsinchu 30013, Taiwan
[b] National Synchrotron Radiation Research Center, Hsinchu 30076, Taiwan
[c] Department of Molecular Science and Engineering, National Taipei University of Technology, Taipei 10608, Taiwan
[d] Department of Greenergy Technology, National University of Tainan, Tainan 7005, Taiwan
[e] Advanced Lithium Electrochemistry Co., Ltd., Taoyuan 33048, Taiwan

HIGHLIGHTS

- Using *in-situ* XRPD, the structure of vanadium (V) added LiFePO$_4$ is elucidated.
- Chemical composition of LiFePO$_4$ changes are revealed by *in-situ* XANES.
- By V adding, the disordered and inactive triphylite phases are reduced.
- The remnant heterosite phase can be reduced by V adding.

GRAPHICAL ABSTRACT
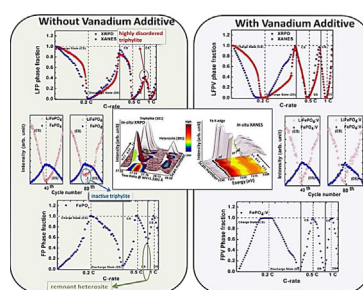
ABSTRACT

The influences of adding vanadium to the structure evolution and electrochemical performance of LiFePO$_4$ are systematically investigated by *in-situ* X-ray powder diffraction and X-ray absorption near edge structure spectroscopy. The results indicate that the addition of a small amount of vanadium (less than at 1%) significantly reduces the formation of non-crystalline (highly disordered) triphylite and remnant heterosite phases in the cathode of battery especially at the rate capability higher than 0.5C. The cycle stability of LiFePO$_4$ cathode with vanadium additive after 80 cycles is improved by 14.9% compared to that without vanadium additive. Such an enhancement could be attributed to the ion diffusion kinetics being improved and inactive triphylite being reduced by the supervalent-vanadium additive in cathode during electrochemical redox cycles.

© 2014 Elsevier B.V. All rights reserved.

1. Introduction

Olivine structured LiFePO$_4$ (LFP) [1,2] is gaining increasingly attention in both academic and industrial communities due to its appealing electrochemical features, including excellent chemical

* Corresponding author. Department of Engineering and System Science, National Tsing Hua University, Hsinchu 30013, Taiwan. Tel.: +886 3 5715131x34281; fax: +886 3 5720724.
E-mail addresses: chlee@mx.nthu.edu.tw, chihhaolee@gmail.com (C.-H. Lee).

and thermal stability, low material cost, non-toxicity as well as a high theoretical capacity for a lithium ion battery (LIB). The rate capability, however, is restricted by the intrinsic natures of low electronic conductivity and poor ionic transport properties which inhibit their widespread conventional applications. These unfavorable electrochemical properties of pristine LFP need to be improved for their practical commercialization especially at the higher C-rates (>5C). Doping with supervalent-cation (Zr, Nb, V, Cr, and Ni etc.) has been proved an efficient way to improve the electrochemical performance (including the intrinsic electronic conductivity, the Li-ion diffusivity, and the durability, etc.) in the LFP [3–11]. The famous examples are that the aliovalent-vanadium (V) doping enhances the rate capability and low temperature performance of LFP. Such type of enhancement can be rationalized by the formation of conductive composition, such as V_2O_3 [12], $Li_3V_2(PO_4)_3$ [13] or enlarged lattice volume [14] for a better Li ion transfer [15].

In addition to the impact of aliovalent-vanadium doping, the structure phase transition mechanisms of the LFP-based cathode materials also provides important information in the performance of LIB. This phenomenon has been extensively studied by using *in-situ* characterizations on the $LiCoO_2$ system in the literature [16,17], where the phase transition is predominated by a solid solution of $Li_{1-y}CoO_2$ during the charge/discharge cycles. Unlike $LiCoO_2$, the phase transition of LFP processes is in a two phase reaction which makes it attractive. In LFP system, the extraction and insertion of lithium-ion in the electrode trigger a structure transition of cathode between the triphylite (LFP) and heterosite ($FePO_4$; FP) phases during the charge/discharge of LIB. The explanation on the fundamental mechanism is still in debating, though the phase transitions are evident. The first core shell (shrinking-core) model, for example, was proposed by Padhi et al., in 1997 [1]. A shrinking-core with a formation of an FP shell was proposed in this model, in which the LFP/FP interface migrates deeply into the particle from the surface with a continuous shrinking of the LFP core upon charging and in the reverse direction upon discharging. Though this model can fit most of the experimental results quite well, however, none of information is provided to explain the ionic diffusion kinetics between different facets in LFP crystallites. This model has thus extensively studied with wider scope by incorporating new boundary conditions, such as the mosaic model [18], the single phase kinetic models [19], and the domino-cascade model [20]. To solve the discrepancies among different models and experimental results, more systematic kinetics experiments on the LFP/FP phase transition are needed.

In previous studies [21–25], the kinetics of microstructure phase transition was investigated by synchrotron X-ray and neutron diffraction at the *in-situ* platform. These two techniques mainly illustrate the structure information from the bulk matrix of triphylite (or heterosite) phase with the long range ordered periodic lattices. However, determination of only the long range structural information in a charge/discharge cycling system which is full of defects is not sufficient to elucidate the structural transition comprehensively. The structure evolution in short range ordering (over a range of several atoms) has been the focus in recent years. The changes of chemical states and the lithium ion diffusivity upon charge/discharge cycling have been widely studied by real-time X-ray absorption spectroscopy (XAS) [26–28]. In this work, we utilize the *in-situ* X-ray absorption near edge structure (XANES) on probing the changes of chemical states around Fe atoms in the short-range order regime in the charge/discharge cycling at different rates. In our previous studies [29,30], we employed the X-ray techniques and neutron powder diffraction (NPD) to depict that the structure change of generating Li vacancy by vanadium substitution, which could enhance the lithium ion

diffusion and thus improve the LIB performance. In this study, we demonstrate a systematic correlation between the phase transformation and electrochemical properties by *in-situ* XRPD and XANES at room temperature. The samples we studied are LFP and LFPV (LiFePO$_4$:VO$_x$) based cathode materials in a punch type cell (lithium foil anode; $LiFePO_4$ or $LiFePO_4$:VO$_x$ cathode). We will emphasize on studying the effect of vanadium additive on the LFP cathode. Our results complementally clarify the crystal structure change and rationalize the enhancement of electrochemical delithiation (charge)/lithiation (discharge) performance on LFP in terms of local chemical standpoint. To shoot the target, the remnant FP, highly disordered LFP, and inactive LFP were simultaneously characterized during LIB charge/discharge cycles at different C-rates and cycles.

2. Experimental

2.1. Sample preparation

The cathode materials of LFP and LFPV were obtained from Advanced Lithium Electrochemical Co., Ltd. (ALEEES). The LFPV powders with 5 mol% vanadium relative to Fe were synthesized via a sol–gel method. Briefly, LiOH·H$_2$O (99.9%, Aldrich), FeC$_2$O$_4$·2H$_2$O (99%, Aldrich), NH$_4$·H$_2$PO$_4$ (97%, Aldrich), and V$_2$O$_5$ (99%, Aldrich) in stoichiometric ratio were dissolved in deionized water. Citric acid was then added into the above solution. The resulting stable suspension was mixed with 5 wt% sucrose and spray-dried in a hot air stream with an inlet pressure of 0.2 MPa. Inlet and outlet temperatures of the dryer were 220 °C and 100 °C respectively. The as-prepared powders were sintered at 800 °C for 12 h in nitrogen atmosphere.

The pouch types of LFP and LFPV based LIBs (half-cell) were prepared with lithium metal as anode; the electrolyte was 1 M LiPF$_6$ in a 1:1 mixture of dimethyl carbonate and ethylene carbonate. The cathodes slurries were made by dispersing of active materials, Super p, and polyvinyl difluoride at a weight ratio of 85:6:9 and coated onto the aluminum foils. Afterward, the cathodes were dried in a vacuum oven at 120 °C for 10 h. The cathode foils are around 50 μm thick and contained approximately 6.5 mg cm^{-2} of the active materials. The cell's dimensions are 1 mm thick × 65 mm wide × 80 mm high. Before the real-time data collection, the batteries were operated between 2.5 V and 4.2 V at a constant current of 2 mA, which corresponds to 0.1C. At such a low C-rate pre-discharge process, the lithium ions were slowly diffused/relocated into the FP crystal to transform the cathode into the LFP phase.

2.2. Material characterization

High-resolution neutron powder diffraction patterns were collected on Echidna beamline at OPAL reactor in Australian Nuclear Science and Technology Organisation (ANSTO) [31], Australia. The neutron wavelength of 2.43950(0) Å was calibrated against the NIST Al$_2$O$_3$ SRM 676 standard. The crystal structure studied was refined by a GSAS/EXPGUI package [32].

The *in-situ* XRPD experiment was performed with a high throughput two-dimensional image plate detector at beamlines of BL07A [33] and BL17A of National Synchrotron Radiation Research Center (NSRRC), Taiwan. The incident X-ray wavelength was calibrated using the AgSi standard powder at the beginning of each experiment. For obtaining the adequate signal to noise ratio and the time resolution, each diffraction pattern was successively collected with an interval of 3 min. The XRPD peak fits were undertaken in the Large Array Manipulation Program (LAMP) [34] using a Gaussian-like shape peak with an adjustable flat background.
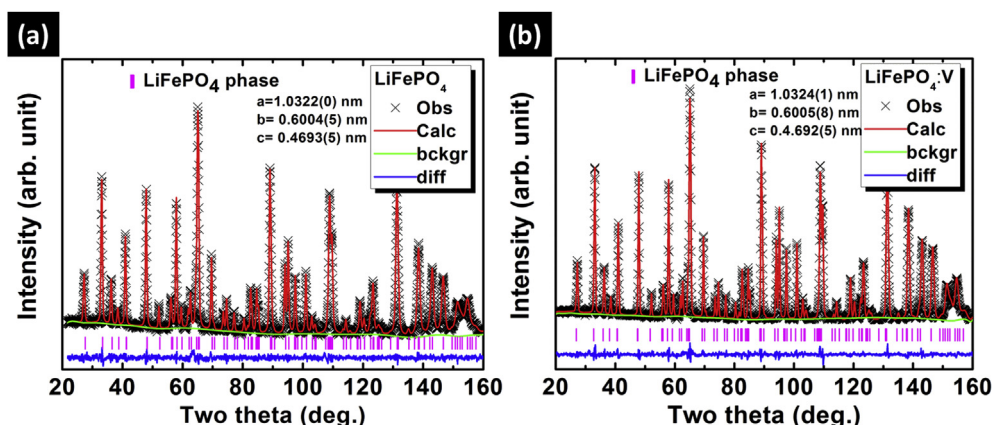
Fig. 1. The results of the Rietveld refinement of NPD pattern of (a) LFP and (b) LFPV. The vertical pink bars indicate Bragg reflections corresponding to an Olivine LFP structure phase. The differences between observed data (shown as cross) and calculated models (shown in red lines) are plotted at bottom as blue lines. The backgrounds are shown in green solid lines. (For interpretation of the references to color in this figure legend, the reader is referred to the web version of this article.)

In-situ Fe *K*-edge XANES characterization was performed at NSRRC beamline BL17 C. The monochromator was scanned in energy from 50 eV below to 600 eV above the Fe K absorption edge (about 7112 eV) with transmission mode measurement. The spectra were analyzed using the Athena 0.8.056 program in the IFEFFIT 6.0 software; where the energy calibration, background subtraction, data normalization, and linear combination fitting were conducted following the standard data interpretation procedures [35].

3. Results and discussion

The initial crystal structure of the LFP with and without vanadium additive is considered as the fundamental information for scrutinizing structure evolutions during the charge/discharge cycling of LIB. In order to understand the positions of Li atoms and Li vacancies of LFP and LFPV, neutron powder diffraction was employed to determine the crystal structure at beginning. The neutron diffraction patterns of the pristine LFP powder with and without vanadium together with the corresponding fitting curves of the Rietveld refinement are illustrated in Fig. 1. No impurity phase (for instance, FeP_4, $Li_3V_2(PO_4)_3$, or LiV_2O_5) is found in diffraction patterns and the corresponding Bragg diffraction peaks are indexed as an olivine-type structure with a Pnma space group. The lattice parameters of the LFP and LFPV obtained by Rietveld refinement analysis are listed in Table 1. Accordingly, the lattice parameters of the pristine LFP possess are $a = 10.322(0)$ Å, $b = 6.004(5)$ Å, and $c = 4.693(5)$ Å, and the volume of unit cell (V) is 290.895(9) Å^3. For

the LFPV samples, the lattice structure of the LFPV was derived by employing the LFP model with vanadium replacement at Li site ($Li_{1-x}V_xFePO_4$, $x \sim 0.75\%$) [29,30]. As shown in Table 1, no significant change on the lattice parameters are found for the LFPV ($a = 10.324(1)$ Å, $b = 6.005(8)$ Å, $c = 4.692(5)$ Å, $V = 290.957(3)$ Å^3) compared to that of LFP. In addition, the density of Li vacancy ($V_{Li}^{''''}$) for the LFPV was determined to be 3.0% ($\pm 0.5\%$), which is approximately 3-folds higher than that of LFP. Although the optimized Li vacancy density for the LIB performances remain to be clarified, this structural evidence together with the electrochemical characterizations (will be disclosed in the later sections) shows that the V additives will create a certain extent of easy ion diffusion channels. Therefore, it is expectable to see the transition between triphylite and heterosite phases during the charge/discharge cycling will be more facilitated by a cathode with vanadium additive.

After the initial crystal structure was determined, the impacts of electrochemical interactions (i.e., the cycle rate and the cycle time) on the crystal phase transformation of LFP and LFPV in a LIB were investigated via synchrotron *in-situ* XRPD instead of using neutron diffraction, because high intensity incident beam is requested for collecting a sufficient amount of scattering intensity within low statistic error, especially, in the cases of C-rates. The *in-situ* XRPD patterns for the LFP and LFPV cathode were conducted at three types of charge–discharge rates as 0.2C, 0.5C and 1C (see Fig. 2 from bottom to top). The sequential cycling potential for charge/discharge is between 2.5 V and 4.2 V as shown in the right panels of Fig. 2(a) and (b). Diffraction patterns are shown at central panels of

Table 1
Rietveld refinement results of LFP and LFPV.

Sample	LiFePO$_4$ (space group: Pnma)				LiFePO4:V (space group: Pnma)			
Lattice volume (Å^3)	$a = 10.322(0)$ Å, $b = 6.004(5)$ Å, $c = 4.693(5)$ Å, 290.895(9)				$a = 10.324(1)$ Å, $b = 6.005(8)$ Å, $c = 4.692(5)$ Å, 290.957(3)			
$V_{Li}^{''''}$ (%)	<1.0				3.0 ± 0.5			
Reliability factors	$R_{wp} = 2.37\%$, $R_p = 2.00\%$				$R_{wp} = 2.86\%$, $R_p = 2.35\%$			
	$\chi^2 = 1.12$				$\chi^2 = 1.50$			
Atoms	x	y	z	Occupancy	x	y	z	Occupancy
Li	0	0	0	1	0	0	0	0.965(6)
Fe	0.282(3)	1/4	0.973(2)	1	0.282(2)	1/4	0.974(2)	1
P	0.095(8)	1/4	0.415(1)	1	0.095(4)	1/4	0.416(2)	1
O(1)	0.096(5)	1/4	0.742(6)	1	0.096(7)	1/4	0.744(4)	1
O(2)	0.457(4)	1/4	0.206(4)	1	0.457(7)	1/4	0.205(9)	1
O(3)	0.166(7)	0.046(3)	0.284(1)	1	0.165(9)	0.047(1)	0.284(9)	1
V					0	0	0	0.0075

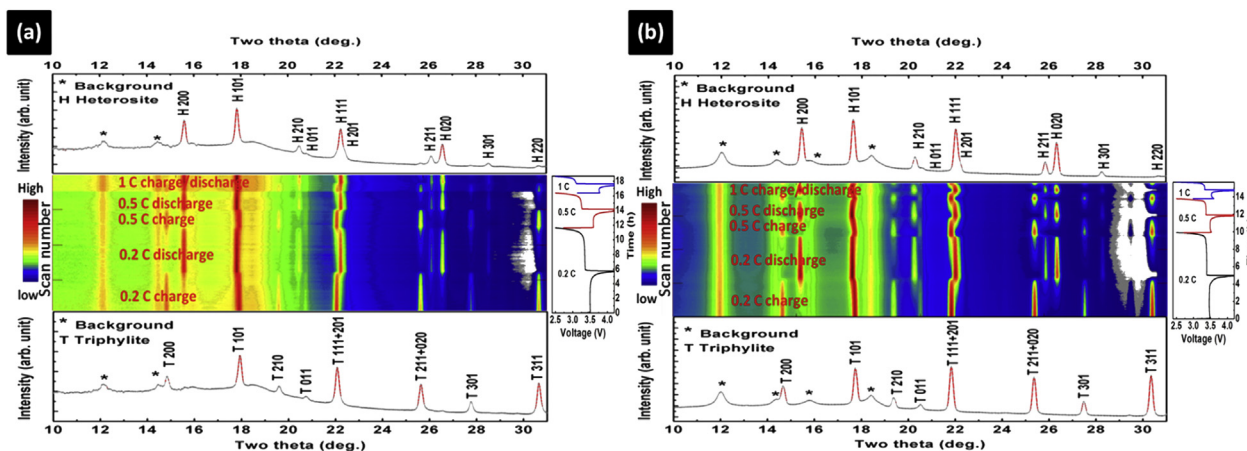$V_{Li}^{''''}$: Li vacancy in bulk structure determined by neutron powder diffraction.

Fig. 2. *In-situ* XRPD patterns for the LFP cathode (a) without and (b) with V additives under successive 0.2C, 0.5C, and 1C (from bottom to top) charge/discharge cycling. The sequential cycling potential for charge/discharge is shown in the right panels of (a) and (b). Diffraction patterns are shown at central panels of (a) and (b) where the intensities are labeled in color levels with the color bars at left hand sides. The lower panels and upper panels show the diffraction patterns of initial triphylite and final heterosite structures, respectively. The background diffraction peaks are mainly due to packing materials. (For interpretation of the references to color in this figure legend, the reader is referred to the web version of this article.)

Fig. 2(a) and (b) with the intensities labeled in color levels. From Fig. 2 we can see that the diffraction patterns change between triphylite and heterosite phases during the charge–discharge processes. To further describe the structure evolution, the diffraction peaks were fitted by the LAMP program with a batch of analyzing functions.

Fig. 3(a) and (b) illustrates the evolution of peak intensities of (301) of LFP/FP and LFPV/FPV at different C-rates (0.2C, 0.5C and 1C), respectively. Fig. 3(a) shows the potential curves and the relative variation of LFP and FP phase fractions during charge and discharge processes. The phase fractions of LFP and FP are obtained from the integrated peak area of (301) reflections relative to that at the beginning of charging and discharging of 0.2C. Because the phase evolution is nearly reversible at 0.2C, the phase fraction of LFP and FP of 0.2C can be considered as reference points to estimate the phase fractions at different C-rates. In Fig. 3(a), significant portions of the FP phase remnants are found for 0.5C and 1C suggesting that the uncompleted charge/discharge cycles are evident by further increasing the C rate. These results indicate that the remnant FP phases are easily formed when lithium ions are inserted into LFP under higher C-rate discharge process. On the other hand, as shown in Fig. 3(b), such remnant phenomenon is almost

absent in LFPV indicating an easy triphylite and heterosite phase transformation.

In order to portrait the full structure evolution scheme, the *in-situ* XANES was employed to obtain the changes of electronic structure on these two cathodes upon charge/discharge cycling. Fig. 4, Fig. S1, and S2 (in ESI) show the *in-situ* Fe K-edge XANES spectra for the LFP and LFPV cathodes in LIB during 0.2C, 0.5C, and 1C electrochemical process. Clean isosbestic points [36] are observed in the real-time absorption spectra which is a direct indication of two mixed phase. It also shows two phase transition mechanism on the delithiation/lithiation reaction of LFP (LFPV). In Fig. 4, the energy shift of the absorption edge (D) is proportional to the oxidation state of Fe. The adsorption edge of Fe shifts to the higher energy as the voltage of cell increases. This indicates a transformation of Fe(II) into Fe(III), which corresponds to the phase transition from LFP to FP upon the delithiation process. During the lithiation (discharge) process, the changes of Fe oxidation states are reversible. The chemical oxidations states at different C-rates and different charge/discharge states of LFP and LFPV half-cells are summarized in Table 2. For the case of low C-rate (see Fig. S1(a)), the position of D is found shifting reversibly from 7123.7 to 7127.5 eV in a single charge–discharge cycle. This suggests a
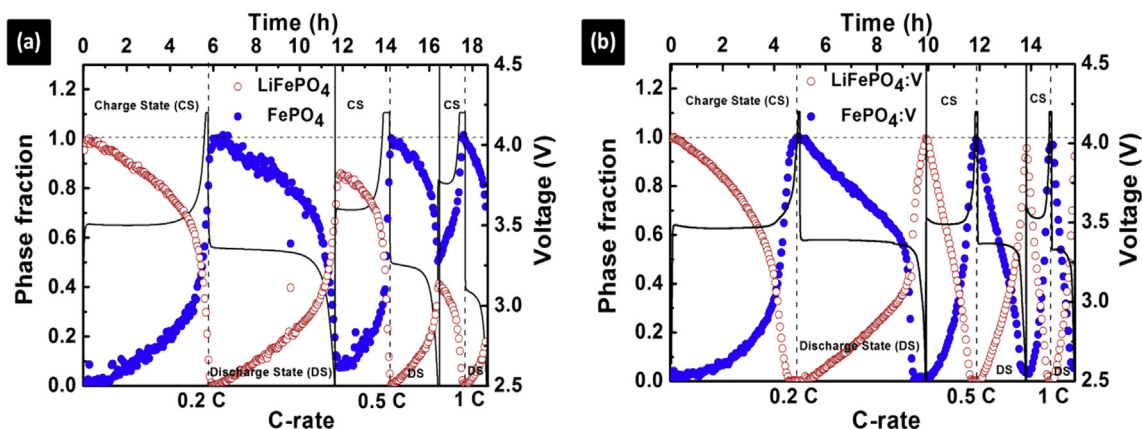

Fig. 3. The changes of phase fractions of (a) LFP/FP and (b) LFPV/FPV estimated from *in-situ* XRPD patterns at 0.2C, 0.5C, and 1C charge/discharge rates. The corresponding electrochemical charge/discharge curves are denoted by solid lines. CS denotes charging cycle and DS denotes discharging cycle.
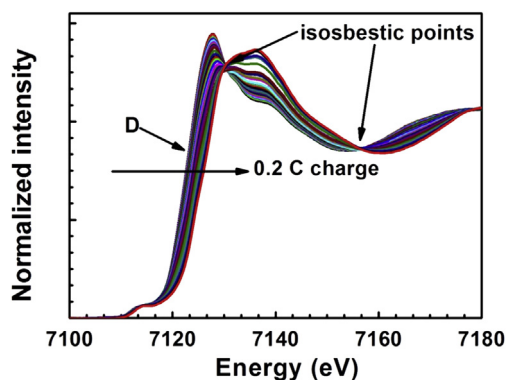
Fig. 4. The normalized *in-situ* Fe *K*-edge XANES spectra at 0.2C charge rate. *D* is the position of absorption edge of each XANES spectrum.

reversible chemical state transition of Fe ions in LFP during deli-thiation and lithiation process. The range of energy shift of *D* is progressively narrowed from 3.8 eV to 2.3 eV by increasing the C rate from 0.2C to 1.0C. The Fe oxidation states before charge of LFP from 0.2C to 1.0C were increased from 2.18 to 2.43. This implies the irreversible chemical redox reaction with the rapid charge/discharge rates in the LFP cathode. On the other hand, with the vanadium additive, this narrowing phenomenon is almost absent even at high C rates as clearly shown by the range of the edge position (*D*) shift in a complete charge–discharge cycle (see Fig. S2(a)–(f) and Table 2). And, the Fe oxidation states before charge of LFPV from 0.2C to 1.0C were remained at 2.0. Therefore, the chemical environments of LFPV are reversible during the charge/discharge cycling.

To understand the influence of vanadium additive to the chemical state changes of Fe ion in a local structure region (short range ordering) at different C-rates (0.2C, 0.5C, and 1C), the phase fraction changes were estimated by a linear combination function analysis. This estimation was conducted on the XANES spectra of the Fig. S1 and S2. The results are demonstrated in Fig. 5(a) for LFP/FP and Fig. 5(b) for LFPV/FPV, where the corresponding charge/discharge curves between 2.5 V and 4.2 V at different C-rates are denoted by solid line. In Fig. 5, the spectra before charging and with fully charged conditions at 0.2C were selected as the reference spectra for the LFP (LFPV) and FP (FPV) in the linear combination

fitting analysis. As shown in Fig. 5(a), the chemical state of Fe was found symmetrically transferred between LFP and FP during the charge/discharge cycling at low C rate (0.2C). This result indicates equilibrium redox kinetics for the Fe ions to accept and donate the charge to their local coordinates when both LFP/FP phases are driven by a low current density. The redox kinetics of Fe becomes progressively unbalanced by increasing the C-rates higher than 0.5. In this case, the chemical state of Fe ions can be fully converted from LFP to FP when the LIB is fully charged. However, the incomplete chemical state of Fe ions from FP to LFP is found in the subsequent discharge process. Presumably, this unbalanced Fe ion chemical state transition could be attributed to the presence of substantial energy barrier (i.e., SEI layer) that hinders chemical state transition of Fe and the Li ion diffusions between FP and LFP during the charge/discharge cycles of LIB at high C-rate. On the other hand (see Fig. 5(b)), symmetric Fe chemical state transition between LFPV and FP was found even by charging/discharging the LIB cycling at 1.0C. Such a phenomenon providing the direct evidence to prove that the vanadium additive will substantially reduce the energy barrier and thus facilitate the redox chemical kinetics of Fe to accept and donate their valence charge during the chemical state transition between LFPV and FP in a LIB. Accordingly, the profile of local chemical state transition presents a similar fashion to that of the feature in the XRPD analysis (see Fig. 3).

Although the profile of local chemical state transition has a similar feature in the XRPD analysis, it shows a significant higher recovering fraction during the discharge process (see Fig. 6(a)), in the FP to LFP crystalline transition. The extents of reversible LFP estimated from XANES are much higher than those of XRPD analysis; especially the phenomenon is more evident at discharging rates higher than 0.5C. The nearly recovered valence state of Fe is direct evidence that a substantial amount of highly disordered triphylite phase is found after completing a charging and discharging cycle under an uncompleted crystalline phase recovery. On the other hand, with the vanadium additive (see Fig. 6(b)), this phenomenon is not significantly observed, in which the crystalline of triphylite phase can be fully recovered. In addition, it shows that the phase transformation is reversible and can be explained by the formation of easy diffusion pathways in the presence of adequate amount of Li vacancies (vacancy effect) due to the charge balance of supervalent-vanadium incorporation in LFP during the electrochemical redox cycles.

Our *in-situ* XANES and XRPD has clarified that the vanadium additive will facilitate the lithium transport within the cathode materials during electrochemical charging and discharging cycles in LIB at different C rates. It also improves the structural stabilization of cathodes during a pro-long cycling time. Fig. 7 shows the discharge capacity versus cycle number for Li/LFP and Li/LFPV cells at 0.2C rate between 2.5 V and 4.2 V. The cycle stability (CS$_N$) for the half-cell LIB at certain number (*N*) of cycle time is estimated by the following equation:

$$CS_N = 1 - \left(\frac{C_i - C_N}{C_i} \right) \times 100\% \qquad (1)$$

where subscript *N* denotes the cycle number, C_i denotes the initial capacity of LIB at the stable state (denoted by A in Fig. 7), and C_N is the capacity of LIB after *N* cycles. Accordingly, the CS$_{80}$ of LFP is determined to be 82.2%. On the other hand, the CS$_{80}$ of LFPV is determined to be 97.1%, which is about 14.9% improved compared to that of LFP. The corresponding *in-situ* XRPD patterns of LFP and LFPV at 40th and 80th cycle are compared in Fig. 8. As clearly indicated in Fig. 8(a), the LFP (301) intensity remain exists (denoted by the arrow) at fully charged state, which indicates the formation of inactive LFP during charging and discharging cycles in the first 39

Table 2
The measurements of Fe K-edge X-ray absorption for the LFP/Li half-cell under different C-rates and different charge/discharge (delithiation/lithiation) states.

LFP (LFPV)/Li half cell						
C-rate	Charge/discharge state	Absorption edge (eV)		Fe oxidation state[a]		Range of edge shift (eV)	
		LFP	LFPV	LFP	LFPV	LFP	LFPV
0.2	Before charge	7123.7	7123.1	2.18	2.07	3.8	5.0
	After charge	7127.5	7128.1	2.88	3.00		
	Before discharge	7127.4	7128.0	2.86	3.00	3.4	5.0
	After discharge	7123.9	7123.0	2.22	2.04		
0.5	Before charge	7123.9	7123.0	2.22	2.05	3.5	5.0
	After charge	7127.4	7128.0	2.87	2.98		
	Before discharge	7127.4	7128.0	2.86	2.97	2.2	5.0
	After discharge	7125.2	7123.0	2.46	2.06		
1	Before charge	7125.1	7123.0	2.43	2.05	2.3	5.0
	After charge	7127.4	7128.0	2.87	2.97		
	Before discharge	7127.2	7128.2	2.82	3.00	0.6	4.8
	After discharge	7126.6	7123.4	2.71	2.12		

[a] The Fe K-edge XANES spectra of pristine LFP and final FP powder at 0.2C are selected as the reference points of Fe^{+2} and Fe^{+3}, respectively.
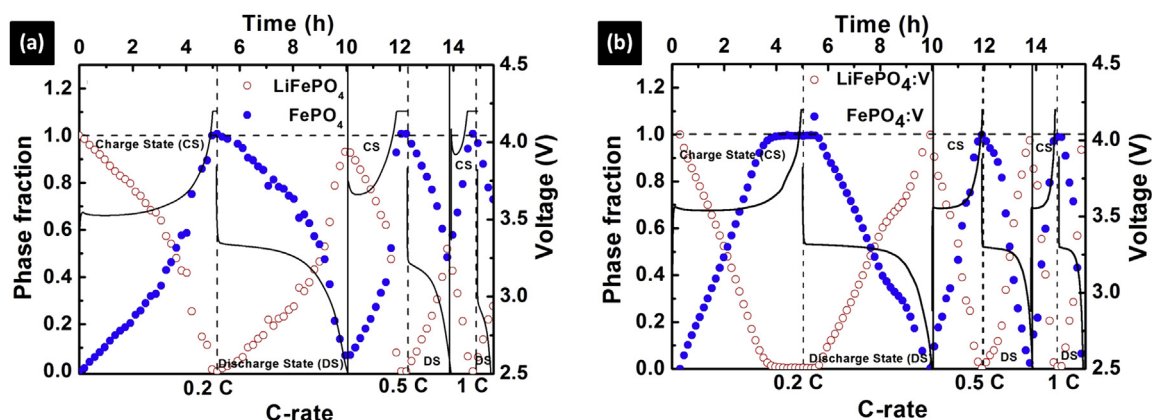
Fig. 5. Results of linear combination fitting analysis of Fe K-edge spectra for (a) LFP/FP and (b) LFPV/FPV under 0.2C, 0.5C and 1C charge/discharge rates. The corresponding electrochemical charge/discharge curves are denoted by solid lines.
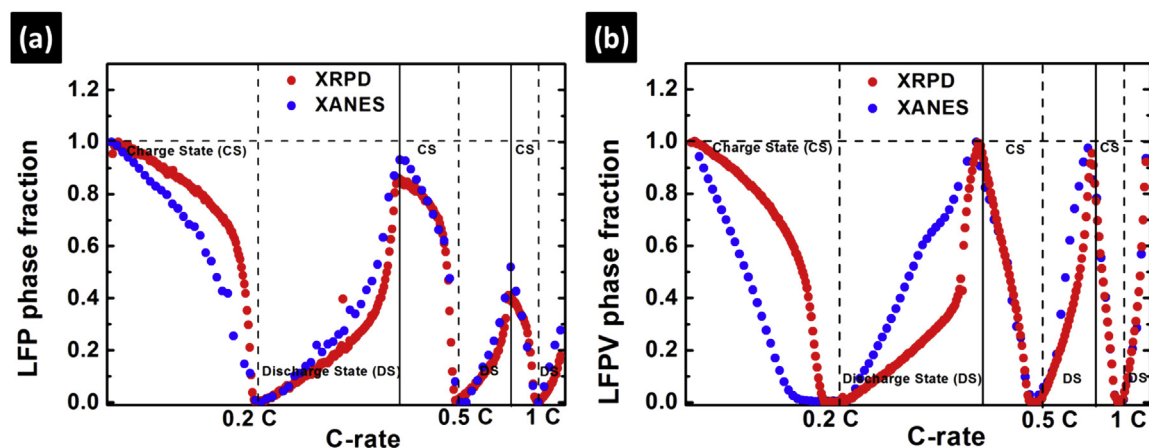

Fig. 6. The relative amounts of (a) LFP and (b) LFPV versus different charge/discharge rates (0.2C, 0.5C, and 1C) as obtained from XRPD data and XANES data.

cycles. This inactive LFP becoming more intense by further increasing the number of charge/discharge cycle up to 80 indicates its irreversibility during the charge/discharge cycling. On the other hand (see Fig. 8(b)), the inactivated component is not as large as that for the vanadium adding LFP.

From half-cell LIB testing results, we found that the amount of inactive LFP phase is sequentially increased by increasing charge/discharge cycle time. For the LFP without adding vanadium, the
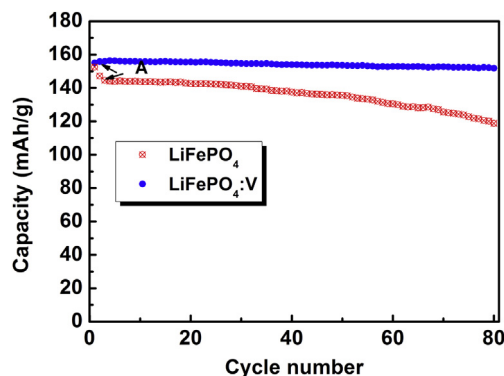
amounts of heterosite in LFP are 8%, 51%, 72% (see Fig. 3(a) at the end of discharge under 0.2C, 0.5C, and 1C rate, respectively. In addition, the formation of highly disordered LFP phase is also related to C-rate. During the discharge process, the higher discharge rate the more the highly disordered LFP phase is formed. This irreversible LFP to FP phase transition, resulting in the capacity losses during charge/discharge cycle. On the contrary, the remnant effects are insignificant for the case of LIB with LFPV cathode (remnant heterosite in LFPV are 1.4%, 2.8%, 5.2% at the end of discharge under 0.2C, 0.5C, and 1C rate respectively (see Fig. 3(b))). These values are significantly smaller than that in LFP without adding vanadium. It indicates that the substantial reversible chemical and structure of LFPV in the absence of highly disordered triphylite phase during the redox reactions.

In summary, we show that defects of LFP including the formation of highly disordered LFP, inactive LFP, and the remnant FP during the charge/discharge cycle processes can be significantly reduced by the vanadium additive. To the best of our understanding, the present result is the first demonstration of revealing the role of vanadium additives in the LFP in an operational LIB from the local chemical state and the crystal structure standpoints. Presumably the supervalent-vanadium additive activates the vacancy effects in cathode during electrochemical redox cycles. These vanadium additive may incorporate into the Li sites of the olivine structure and lead to a formation of excess vacancies [29] to enhance the fast transport of Li ions. Therefore, the formation of
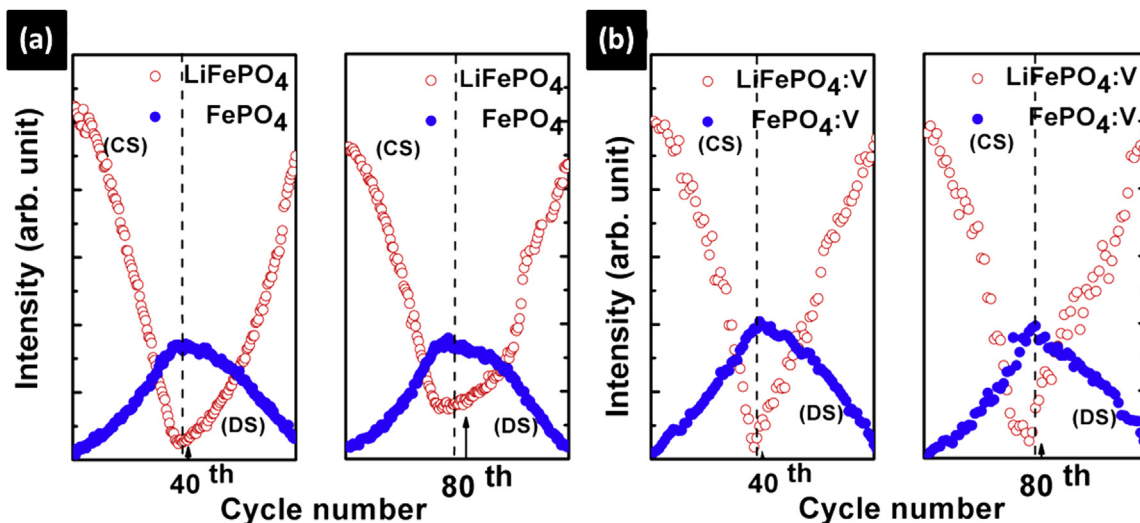

Fig. 7. Cycling performances of LFP and LFPV at 0.2C rate between 2.5 V and 4.2 V at room temperature.

Fig. 8. The intensity variations of (301) peak of (a) LFP/FP and (b) LFPV/FPV under 40th and 80th charge/discharge cycling. CS denotes charging cycle and DS denotes discharging cycle.

inactive LFP phase is significantly reduced and prolongs the cycle life of LIB at higher C-rates substantially.

4. Conclusions

The cathode materials of LFP with and without vanadium additive for lithium-ion battery are investigated by using a long range ordered *in-situ* XRPD and a short range ordered Fe *K*-edge XANES techniques. By a small amount of vanadium additive, the highly disordered triphylite phase, the inactive triphylite phase, and the remnant heterosite phase are significantly reduced especially under higher C-rate cycling or after cycling many times. Meanwhile, it improves the structural reversibility of LIB between the heterosite and triphylite phase transitions. Most importantly, the full scope structural characterization of this work has outlined a necessary correlation to improve electrochemical stability for the frontier design of future LIB applications.

Appendix A. Supplementary data

Supplementary data related to this article can be found at http://dx.doi.org/10.1016/j.jpowsour.2014.07.138.

References

[1] A.K. Padhi, K.S. Nanjundaswamy, J.B. Goodenough, J. Electrochem. Soc. 7 (1997) 1188–1194.
[2] J. Chen, M.S. Whittingham, Electrochem. Commun. 8 (2006) 855–858.
[3] F. Omenya, N.A. Chernova, R. Zhang, J. Fang, Y. Huang, F. Cohen, N. Dobrzynski, S. Senanayake, W. Xu, M.S. Whittingham, Chem. Mater. 25 (2013) 85–89.
[4] J. Molenda, A. Kulka, A. Milewska, W. Zając, K. Świerczek, Mater. 6 (2013) 1656–1687.
[5] Y.B. Cao, L. Luo, K. Du, Z.D. Peng, G.R. Hu, F. Jiang, Acta Phys. Chim. Sin. 29 (2013) 1507–1514.
[6] Y. Ge, X. Yan, J. Liu, X. Zhang, J. Wang, X. He, R. Wang, H. Xie, Electrochim. Acta 55 (2010) 5886–5890.
[7] H.C. Shin, S.B. Park, H. Jang, K.Y. Chung, W.I. Cho, C.S. Kim, B.W. Cho, Electrochim. Acta 53 (2008) 7946–7951.
[8] K.L. Harrison, C.A. Bridges, M.P. Paranthaman, C.U. Segre, J. Katsoudas, V.A. Maroni, J.C. Idrobo, J.B. Goodenough, A. Manthiram, Chem. Mater. 25 (2013) 768–781.
[9] Y.W. Chen, J.S. Chen, Int. J. Electrochem. Sci. 7 (2012) 8128–8139.
[10] F. Omenya, N.A. Chernova, Q. Wang, R. Zhang, M.S. Whittingham, Chem. Mater. 25 (2013) 2691–2699.
[11] F. Omenya, N.A. Chernova, S. Upreti, P.Y. Zavalij, K.-W. Nam, X.-Q. Yang, M.S. Whittingham, Chem. terials. 23 (2011) 4733–4740.
[12] Y. Jin, C.P. Yang, X.H. Rui, T. Cheng, C.H. Chen, J. Power Sources 196 (2011) 5623–5630.
[13] X.D. Guo, B.H. Zhong, H. Liu, Y. Song, J.J. Wen, Y. Tang, Trans. Nonferrous Met. Soc. China 21 (2011) 1761–1766.
[14] H. Liu, Q. Cao, L.J. Fu, C. Li, Y.P. Wu, H.Q. Wu, Electrochem. Commun. 8 (2006) 1553–1557.
[15] H. Liu, C. Li, Q. Cao, Y.P. Wu, R. Holzw, J. Solid State Electrochem. 12 (2008) 1017–1020.
[16] C.N. Li, J.M.M. Yang, V. Krasnov, J. Arias, K.W. Nieh, Electrochem. Solid-State Lett. 11 (2008) A81–A83.
[17] Z. Chen, Z. Lu, J.R. Dahn, J. Electrochem. Soc. 149 (2002) A1604–A1609.
[18] A.S. Andersson, J.O. Tomas, J. Power Sources 97-98 (2001) 498–502.
[19] R. Malik, F. Zhou, G. Ceder, Nat. Mater. 10 (2011) 587–590.
[20] C. Delmas, M. Maccario, L. Croguennec, F.L. Cras, F. Weill, Nat. Mater. 7 (2008) 665–671.
[21] A.S. Andersson, B. Kalska, L. Häggström, J.O. Thomas, Solid State Ionics 130 (2000) 41–52.
[22] N. Sharma, V. Peterson, J. Solid State Electrochem. 16 (2012) 1849–1856.
[23] Y. Orikasa, T. Maeda, Y. Koyama, T. Minato, H. Murayama, K. Fukuda, H. Tanida, H. Arai, E. Matsubara, Y. Uchimoto, Z. Ogumi, J. Electrochem. Soc. 160 (2013) A3061–A3065.
[24] X.-J. Wang, C. Jaye, K.-W. Nam, B. Zhang, H.-Y. Chen, J. Bai, H. Li, X. Huang, D.A. Fischer, X.-Q. Yang, J. Mater. Chem. 21 (2011) 11406–11411.
[25] Y. Orikasa, T. Maeda, Y. Koyama, H. Murayama, K. Fukuda, H. Tanida, H. Arai, E. Matsubara, Y. Uchimoto, Z. Ogumi, Chem. Mater. 25 (2013) 1032–1039.
[26] A. Deb, U. Bergmann, S.P. Cramer, E.J. Cairns, Electrochim. Acta 50 (2005) 5200–5207.
[27] X. Yu, Q. Wang, Y. Zhou, H. Li, X.-Q. Yang, K.-W. Nam, S.N. Ehrlich, S. Khalid, Y.S. Meng, Chem. Commun. 48 (2012) 11537–11539.
[28] X. Yu, Q. Wang, Y. Zhou, H. Li, X.-Q. Yang, K.-W. Nam, S.N. Ehrlich, S. Khalid, Y.S. Meng, Chem. Commun. 48 (2012) 11537–11539.
[29] C.Y. Chiang, H.C. Su, P.J. Wu, H.J. Liu, C.W. Hu, N. Sharma, V.K. Peterson, H.W. Hsieh, Y.F. Lin, W.C. Chou, C.H. Lee, J.F. Lee, B.Y. Shew, J. Phys. Chem. C 116 (2012) 24424–24429.
[30] C.W. Hu, N. Sharma, C.Y. Chiang, H.C. Su, V.K. Peterson, H.W. Hsieh, Y.F. Lin, W.C. Chou, B.Y. Shew, C.H. Lee, J. Power Sources 244 (2013) 158–163.
[31] K.D. Liss, B.A. Hunter, M.E. Hage, T.J. Noakes, S.J. Kennedy, Phys. B 385–386 (2006) 1010–1012.

[32] B.H. Toby, J. Appl. Crystallogr. 34 (2001) 210—213.
[33] S.H. Chang, C.H. Chang, J.M. Juang, L.J. Huang, T.F. Lin, C.F. Chang, D.G. Liu, K.L. Tsang, W.F. Pong, C.H. Du, S.L. Chang, Y.L. Soo, M.T. Tang, Chin. J. Phys. 50 (2012) 220—228.

[34] D. Richard, M. Ferrand, G.J. Kearley, J. Neutron Res. 4 (1996) 33—39.
[35] B. Ravel, M. Newville, J. Synchrotron Radiat. 12 (2005) 537—541.
[36] A.D. McNaught, A. Wilkinson, Compendium of Chemical Terminology, second ed., Blackwell Scientific Publications, Oxford, UK, 1997.